Doping Dependent T_c Anisotropy and Coherence Length Measurements in LSCO

Itay Mangel

Doping Dependent T_c Anisotropy and Coherence Length Measurements in LSCO

Research Thesis

In Partial Fulfillment of The Requirements for the Degree of Master of Science in Physics

Itay Mangel

Submitted to the Senate of the Technion - Israel Institute of Technology

Elul, 5779, Haifa, September, 2019

The Research Thesis was done under the supervision of Professor Amit Keren in the Department of Physics.

The generous financial help of the Technion is gratefully acknowledged

Contents

List of Figures

Abstract

The superconducting stiffness $\hat{\rho}_s$relates between a vector potential $\boldsymbol{A}$ and the current density $\boldsymbol{J}_s$ inside superconducting (SC) materials as described by the London equation $\boldsymbol{J}_s = -\hat{\rho}_s \boldsymbol{A}$. The coherence length ξ is a measure of how large can $\boldsymbol{J}_s$ be. A new way of measuring the superconducting stiffness and coherence length using a Stiffnessometer was developed [1] in our group. The measurement is done by applying current in a thin and long excitation coil that pierces a SC ring-shaped sample and creates a rotor-free vector potential $\boldsymbol{A}$ inside the sample. According to London's equation, SC currents emerge leading to a magnetic moment, which is measured using a superconducting quantum interference device (SQUID). The new method does not suffer from demagnetization factors complications or the presence of vortices. The method was applied to $La_{2-x}Sr_xCuO_4$ (LSCO), a member of the cuprates. The crystalline structure of LSCO is roughly tetragonal, with two symmetric directions (a and b) parallel to the CuO_2 planes and the c direction perpendicular to the planes. Consequently, the stiffness is anisotropic, and one might expect different response to a vector-potential $\boldsymbol{A}$ parallel or perpendicular to the planes. Upon warming, the stiffness signal diminishes and disappears at T_c. Stiffness measurements for two different rings, one with the CuO_2 planes parallel to the ring (c-ring) and another with the planes perpendicular to the ring (a-ring) were done for doping of $x = 12.5\,\%$ [2]. It seems as if the phase transition of the c-ring is taking place

at a temperature 0.7 K higher than the a-ring.

It is not clear if this result is unique to $x = 12.5\,\%$ or a general property of LSCO in all doping. If the transition temperature anisotropy is found only in $x = 12.5\,\%$ and its vicinity, it means that the phenomena is related to charge ordering found in this doping. If the T_c anisotropy is found in other doping, it must be a general property related to the two dimensional nature of the CuO_2 planes.

In this work I will present stiffness measurements of LSCO a-rings and c-rings with different doping and determine the dependence of this strange anisotropy in T_c on doping. Additionally, by driving the current in the coil until the linearity between $\boldsymbol{A}$ and $\boldsymbol{J}_s$ breaks, the critical-current of the SC can be measured in the absence of vortices and with no leads or out-of-equilibrium conditions. This critical-current places an upper limit on ξ. We performed such a measurement using a NbTi SC coil and overdoped LSCO. We found that $\xi \leq 4\,\mathrm{nm}$. Future improvements in the experimental setup will allow us to place a tighter bound on ξ.

Symbols and Abbreviations

Abbreviations

AF Antiferromagnet

BC Boundary Conditions

CP Cupper-Pair

GFC Gauge Field Cooling

GL Ginsburg Landau

HTSC High Temperature Super Conductors

ID Inner Diameter

JJE Josephson Junction Effect

LSCO $La_{2-x}Sr_xCuO_4$

OD Outer Diameter

OPD Optimally Doped

OVD Over Doped

PDE Partial Differential Equation

QCP Quantum Critical Point

SC Superconductivity

SC superconductor/superconducting

SQUID Superconducting Quantum Interference Device

TSFZ Traveling-Solvent-Floating-Zone

UND Under Doped

ZGFC Zero Gauge-Field Cooling

Symbols

$\boldsymbol{A}$ Vector Potential

A^c Critical Vector Potential

B Total Magnetic Field

x Strontium doping level of $La_{2-x}Sr_xCuO_4$

c Speed of Light

e Electron Charge

H External Magnetic Field

H_{c1} First Superconducting Critical Field

H_{c2} Second Superconducting Critical Field

I Current

$\boldsymbol{J}_s$ Current Density

J_c	Critical current Density
m	Magnetic Moment
m_e	Electron Mass
n	Windind Density of the Excitation Coil
$\hat{\varphi}$	Azimuthal Direction
Φ	Magnetic Flux
φ	Phase of the Complex Order Parameter
Φ_0	Flux Quanta
ψ	Complex Order Parameter
ρ	Resistivity
$\hat{\rho}_s$	Superconducting Stiffness
T	Temperature
T_c	Critical Temperature
T_N	Néel Temperature
$\boldsymbol{v}_c$	Critical Velocity
ξ	Coherence Length

1 Introduction

1.1 Motivation

The LSCO compound is one of the cuprates family and like all cuprates is made up of copper oxide planes. Due to this layered structure, LSCO is strongly an-isotropic. Different experiments were done and indeed found strong an-isotropic behavior by measuring resistance with strong magnetic fields perpendicular to the copper oxide planes [3], or measuring the Meissner effect of thin single-crystal needles with the planes parallel to the needle's axis (a-needle) and needles with the planes perpendicular to the needle's axis (c-needle) [4]. But these results could be explained by a microscopic phenomenon and not necessarily suggest a macroscopic phenomena of bulk superconductivity. To verify this issue, another experiment was done using a novel technique called Stiffnessometer, which can measure the superconducting stiffness of a bulk superconductor. The Stiffnessometer technique will also be explained in this work in details. By measuring two samples of the same single-crystal, but with different orientation of the copper oxide planes, a different critical temperature (T_c) was observed. The most basic principle of this technique is using a long coil to create currents in a ring-shaped sample and measuring the magnetic moment of the induced currents. The results of this experiment are presented in Fig 1.1. The measured sample was under doped LSCO $x = 12.5\,\%$ and the T_c difference was $0.7\,\mathrm{K}$. The main purpose of the present work is to explore the hole-doping dependence of this

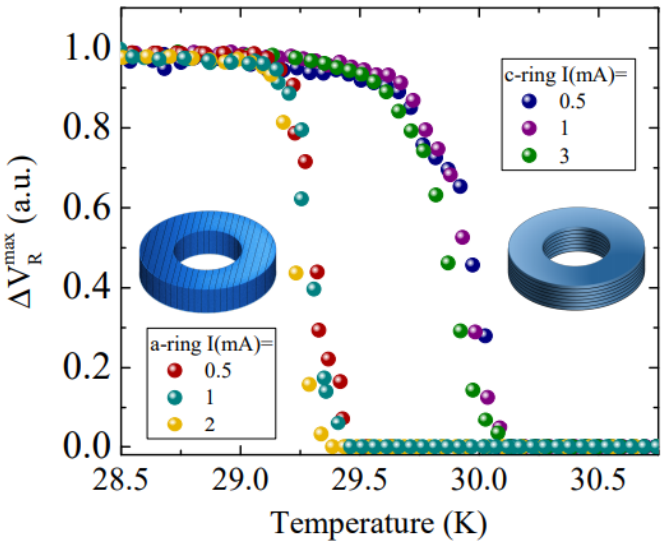

Figure 1.1: Stiffness measurements of LSCO$x = 12.5\,\%$ a and c rings. Explanation about the stiffnessometer can be found in Sec 2.

difference in T_c. Another goal of this work was to measure the coherence length ξ of LSCO at low temperatures ($T \ll T_c$).

1.2 Superconductivity

Superconductivity (SC) is a special phase characterized by many unique phenomena such as zero resistance and perfect diamagnetizem (Meissner Effect). Classical SC can be explained by the BCS-Theory (named for John Bardeen, Leon Cooper, and John Robert Schrieffer), which considers attractive interaction between electrons through electron-phonon coupling. It is common to think of the charge carriers of a SC as pairs of electrons called Cupper-Pairs (CP) rather than individual electrons. The critical temperature T_c refers to

the temperature where the transition between the SC phase and the normal phase happens.

The coherence length ξ is the shortest length scale of over which the phase of the complex order parameter can vary. It is also common to think of ξ as the size of the CP. When applying magnetic field to a SC, it will reject it by creating super currents which screen the external magnetic field. If we increase the external field, the super currents will also increase. Although the field is expelled from the bulk, it penetrates along the edges with exponential decay with some characteristic length known as the penetration depth λ.

The SC materials can be divided into two types depending on the ratio of ξ and λ. Type-I SC have $\lambda < \xi$ and type-II SC have $\lambda > \xi$. A type-I SC will hold the magnetic field outside until we reach the critical field H_c. Above H_c the material gives-up and transforms back to the normal state, letting all the magnetic flux go through it. Type-II SC will stay field free up to some critical field H_{c1}, and above it is capable of letting some of the magnetic flux get in as a vortex. The core of the vortex will be in the normal state phase, but outside of the vortex the material will remain a SC. When we increase the external field, more vortices will get inside until they cover the entire material and all of it becomes normal at a second critical field H_{c2}. In 1986 a new family of SC materials was discovered – the Cuprates. Those materials are defined by having a nearly tetragonal unit cell which form layers of copper-oxygen planes (CuO_2). This SC group will be discussed more in Sec 1.5.

1.3 The London Equation and the Meissner Effect

The superconducting Stiffness $\hat{\rho_s}$ is defined by a local relation between the superconducting current density $\boldsymbol{J}_s$ to the vector potential $\boldsymbol{A}$ and the gradient of φ, the phase of the complex order parameter $\psi = |\psi|e^{i\varphi}$. This relation is:

$$\boldsymbol{J}_s = \hat{\rho_s}(\frac{\hbar c}{q}\boldsymbol{\nabla}\varphi - \boldsymbol{A}). \tag{1.1}$$

where c is the speed of light and q is the charge of the charge carriers. $\hat{\rho_s}$ is a diagonal tensor or even scalar. This equation is gauge invariant. When $\nabla\varphi = 0$ as in our case, we get:

$$\boldsymbol{J}_s = -\hat{\rho_s}\boldsymbol{A}. \tag{1.2}$$

If we use the rotor of Maxwell's equation: $\boldsymbol{\nabla} \times \boldsymbol{\nabla} \times \boldsymbol{B} = \frac{4\pi}{c}\boldsymbol{\nabla} \times \boldsymbol{J}$ (where $\boldsymbol{J}$ is the sum of normal and super currents) and the definition of $\boldsymbol{A}$: $\boldsymbol{B} = \boldsymbol{\nabla} \times \boldsymbol{A}$ we get a partial differential equation for the magnetic field $\boldsymbol{B}$:

$$\boldsymbol{\nabla}^2\boldsymbol{B} = \frac{4\pi}{c}\hat{\rho_s}\boldsymbol{B} \tag{1.3}$$

The solution (in one dimension) will be: $B = B_0 e^{-\frac{x}{\lambda}}$. This exponential decay of the magnetic field inside the bulk of a SC is called The Meissner Effect and it gives us the relation between the SC stiffness and the penetration depth λ:

$$\rho_s = \frac{c}{4\pi}\frac{1}{\lambda^2}. \tag{1.4}$$

1.4 The Ginsburg-Landau Approach

Another way to look at the superconducting phenomena is from the Ginsburg-Landau (GL) point of view (following [5]), denoting the complex SC quantum state as $\psi = |\psi|e^{i\varphi}$ where $|\psi|^2$ is the density and φ is the phase. The GL functional of the free energy is:

$$f = f_{n0} + \alpha|\psi|^2 + \frac{\beta}{2}|\psi|^4 + \frac{1}{2m^*}|(\frac{\hbar}{i}\boldsymbol{\nabla} - \frac{e^*}{c}\boldsymbol{A})\psi|^2 + \frac{(\nabla \times \boldsymbol{A})^2}{8\pi}. \tag{1.5}$$

To minimizes the free energy, we differentiate by ψ^* and it gives:

$$\alpha\psi + \beta|\psi|^2\psi + \frac{1}{2m^*}(\frac{\hbar}{i}\boldsymbol{\nabla} - \frac{e^*}{c}\boldsymbol{A})^2\psi = 0 \tag{1.6}$$

and minimizing with respect to $\boldsymbol{A}$ leads to:

$$\begin{aligned} \boldsymbol{J} &= \frac{c}{4\pi}\boldsymbol{\nabla} \times \boldsymbol{\nabla} \times \boldsymbol{A} \\ &= \frac{e^*\hbar}{2m^*i}(\psi^*\nabla\psi - \psi\nabla\psi^*) - \frac{e^{*2}}{m^*c}\psi^*\psi\boldsymbol{A} \\ &= \frac{e^*}{m^*}|\psi|^2(\hbar\boldsymbol{\nabla}\varphi - \frac{e^*}{c}\boldsymbol{A}) = e^*|\psi|^2\boldsymbol{v}_s \end{aligned} \tag{1.7}$$

where $\boldsymbol{v}_s$ and m^* are the charge carrier's velocity, and mass, e^* is their charge, and $|\psi_\infty|^2$ is their density deep inside the bulk of the SC. We define $f = \psi/\psi_\infty$ and $\psi_\infty^2 = -\alpha/\beta > 0$ which minimize the free energy deep in the SC bulk where $\boldsymbol{A} = 0$ and $\nabla\varphi = 0$. Then, if there are no magnetic fields and $\boldsymbol{A} = 0$,

Eq 1.6 becomes (in one dimension):

$$\frac{\hbar^2}{2m^*|\alpha|}\frac{d^2f}{dx^2} + f - f^3 = 0 \tag{1.8}$$

and we can define the GL coherence length:

$$\xi^2_{(GL)} = \frac{\hbar^2}{2m^*|\alpha|}. \tag{1.9}$$

When we use $\frac{1}{2m^*}(\frac{\hbar}{i}\boldsymbol{\nabla} - \frac{e^*}{c}\boldsymbol{A})^2\psi = \frac{m^*v_s^2}{2|\alpha|}\psi$ in Eq 1.6 we obtain:

$$|\psi|^2 = \psi^2_\infty(1 - \frac{m^*v_s^2}{2|\alpha|}) = \psi^2_\infty[1 - (\frac{\xi m^* v_s}{\hbar})^2] \tag{1.10}$$

$$J_s = e^*\psi^2_\infty(1 - \frac{m^*v_s^2}{2|\alpha|})v_s. \tag{1.11}$$

One can see that J_s as a function of v_s has maximum for a specific velocity. Those are the critical current and the critical velocity:

$$J_c = e^*\psi^2_\infty\frac{2}{3}(\frac{2}{3}\frac{|\alpha|}{m^*})^{1/2}, \tag{1.12}$$

$$v_c = (\frac{2}{3}\frac{|\alpha|}{m^*})^{1/2}. \tag{1.13}$$

Therefore, if we measure the critical velocity v_c, we can also find ξ using the relation:

$$\xi = \frac{\hbar}{\sqrt{3}m^*v_c}. \tag{1.14}$$

If we assume that $m^* = 2m_e$ (m_e being the mass of a free electron) and

$e^* = 2e$ (e being the charge of a free electron) we can find from Eq 1.5 that:, $\beta = |\alpha|\frac{8\pi e^2}{m_e c^2}\lambda^2$, and so $|\psi_\infty|^2 = \frac{m_e c^2}{8\pi e^2 \lambda^2}$. Then using Eq 1.12 we find:

$$J_c = \frac{m_e c^2}{6\pi e \lambda^2} v_c \tag{1.15}$$

In SI units we get:

$$J_c^{\mathrm{SI}} = \frac{2m_e}{3\mu_0 e \lambda^2} v_c \tag{1.16}$$

1.5 The Cuprates Family

The cuprates are a family of High Temperature SC (HTSC) discovered in 1986. They are constructed from planes of copper oxide (CuO_2) with rear-earth metals and oxygen between them. Doping of holes or electrons can be done by adding oxygen or by replacing some of the rear-earth atoms with different atoms with less or more electrons in the valance shell. The LSCO compound ($La_{2-x}Sr_xCuO_4$) is a simple member of this family. It can be hole-doped by replacing some Lanthanum atoms with Strontium atoms (changing x in the compound's formula) and can be SC when x is roughly between $\sim 5\,\%$ and $\sim 27\,\%$. Its highest T_c is about $\sim 38\,\mathrm{K}$ and can be achieved when it is Optimally Doped (OPD) $x \approx 15\,\%$. LSCO with smaller/bigger x is called Under/Over doped (UND/OVD). The unit-cell of LSCO is tetragonal and demonstrated in Fig 1.2.

In general, the cuprates phase diagram is very rich, with many different regimes such as: SC, Antiferromagnet (AF), Fermi Liquid, Strange Metal

and the Pseudogap regime. This work will concentrate on the SC phase. In Fig 1.3 one can see a typical phase diagram of cuprates as a function of doping p. For LSCO $p = x$. When $x = 0$, the material is antiferromagnet with Néel temperature T_N of about $\sim 300\,\mathrm{K}$ and it drops down when increasing x and vanish at $x \approx 2\,\%$. Although the long range order of the AF disappears, short range spin order remains up to $x \approx 12\,\%$ (inside the SC regime). Above T_c in the OPD and UND regime, LSCO behaves as strange metal having linear dependence of the resistivity with temperature ($\rho \propto T$ instead of $\rho \propto T^2$ as normal metal) and when $x > 27\,\%$ LSCO behaves as Fermi liquid. $x \approx 19\,\%$ is called the quantum critical point (QCP). At this point the pseudogap line ends, and the border line between the strange metal phase and the Fermi liquid phase begins [6]. As we shall see, the QCP will be significant in our study.

1.6 Crystal Making

All the samples we used were single crystals of LSCO, which were grown in our lab using the traveling solvent floating zone furnace (TSFZ) technique. At first, all compounds are dehydrated, weighted and mixed together in a process that includes four cycles of mixing and baking. After the four cycles, the powder's homogeneity is checked by x-ray powder diffraction. Then, the powder is inserted into a rubber tube and pressed at 55000 PSI. Out of the rubber tube come rods of condensed powder. The rods are sintered at 1050 c° for 24 hours to form a feed and seed for the TSFZ. The feed rod is

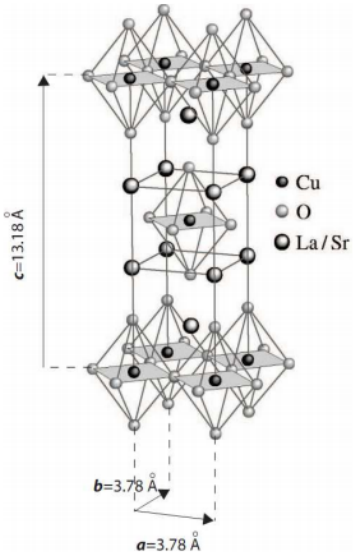

Figure 1.2: LSCO Unit Cell [7].

about $100 - 150$ mm long and is hanged inside a quartz tube. The seed rod is set below the hanged rod. The TSFZ is based on four 300 w lamps and ellipsoid mirrors, which focus the light to the same spot in the gap between the feed and the seed. The power of the lamps is increased until the bottom of the feed and top of the seep are melted to a liquid solvent. The feed and seed are then connected. During this process the feed and seed are rotated in different direction so that the solvent will be homogenize in terms of heat and mixture. The lamps and mirrors are set on a stage that can move up melting more of the feed while the solvent solidify on top of the seed. The feed is also connected to a moving shaft. The quartz tube is sealed and filled with gas with a certain pressure that can be adjust . The operator controls many parameters: the power of the lamps, the moving speed of the mirror

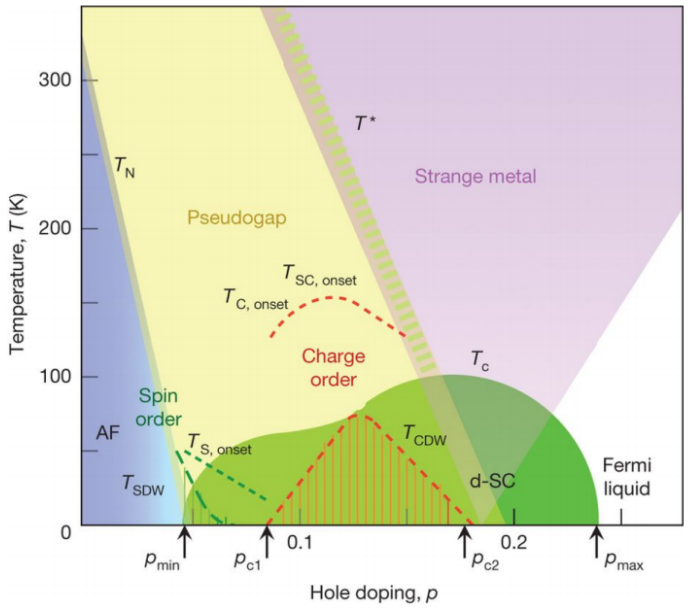

Figure 1.3: Cuprates Phase Diagram of hole doping p and temperature [8].

shaft as well as the feed shaft, rotation speed, the type of gas in the tube and its pressure. The lamp's power is usually high in the beginning of the crystal growth for the first melting of the feed and is slowly reduced until small crystals start to form. This process is done in stages and the end result will depend on the whole process and not only on the end parameters. When the growth program and all the parameters are right, the solvent will solidify as a single crystal. More information on crystal growing can be found in an article by S.M. Koohpayeh et al [9]. A photo of the feed and seed rods, the lamps and mirrors, and the quartz tube is presented in Fig 1.4b. Schematic of the feed and seed rods, the lamps and mirrors, and the quartz tube is presented in Fig 1.4a.

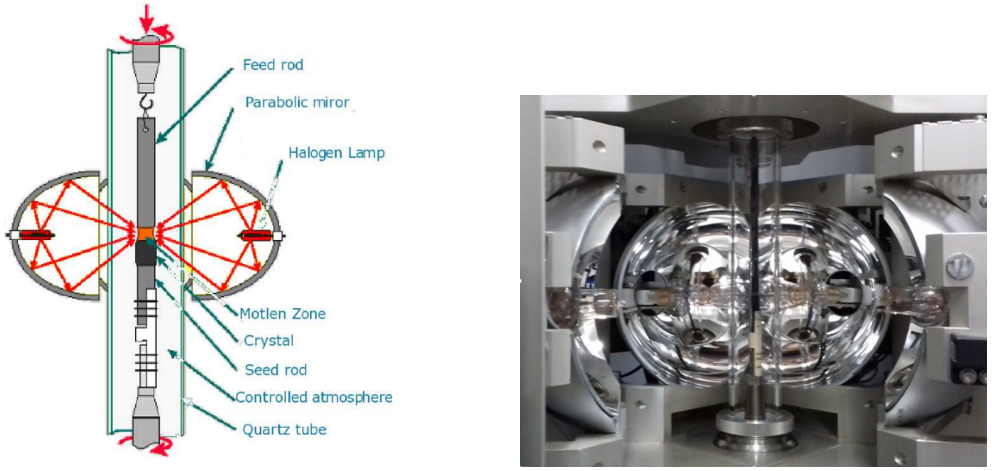

(a) (b)

Figure 1.4: Traveling solvent floating zone furnace. (a) Schematic of the feed and seed rods, the lamps and mirrors, and the quartz tube. (b) Photo of the feed and seed rods, the lamps and mirrors, and the quartz tube.

2 Stiffnessometer Principle of Operation

In this section, we explain the principle of operation of the new device, which we name Stiffnessometer, aimed at measuring stiffness. The ideal Stiffnessometer is made of an infinitely long excitation-coil piercing a ring-shaped sample. When we apply current I through the infinitely long excitation-coil, we can generate a magnetic field inside this coil without a field outside. Nevertheless, there is vector potential $\boldsymbol{A} = \frac{\mu_0 n I}{r}\hat{\varphi}$ where n is the winding density and r is the distance from the coil's symmetry axis. If we cool the sample below T_c without any magnetic field or current in the excitation coil, there will be no vector potential $\boldsymbol{A} = 0$. We call this cooling process Zero-Gauge-Field-Cooling (ZGFC). When we cool the sample and it becomes a SC, it will choose the phase φ to be such that minimize the free energy. Therefore, when we follow the ZGFC protocol, the vector potential is zero $\boldsymbol{A} = \mathbf{0}$ and $\nabla\varphi = 0$ then we get London's equation- Eq 1.2, changing φ is energetically costly for the SC, so when we turn on the current in the coil and $\boldsymbol{A} \neq 0$, we get $\boldsymbol{J}_s = -\hat{\rho}_s \boldsymbol{A}$, meaning that the vector potential $\boldsymbol{A}$ generates super currents $\boldsymbol{J}_s$ inside the ring. Those super currents going around in a loop create a magnetic moment m which can be measured using a pickup-loop connected to a SQUID. The London equation shows linear relation between $\boldsymbol{J}_s$ and $\boldsymbol{A}$. Since $\boldsymbol{A}$ is proportional to the current in the excitation coil I, and $\boldsymbol{J}_s$ is proportional to the sample's magnetic moment m, we get a linear relation between the applied current and the measured signal. When this

linearity breaks, we know that something had changed in the system and we are out of the linear regime.

There are two types of measurements we can do: we can stay at a constant temperature and increase the current I; this type of measurement determines the critical vector potential A^c, hence J_c and ξ. Alternatively, we can change the temperature while the current is in the linear regime and constant; this type of measurement provides the stiffness. We will explain both options in sections 2.6 and 2.5. Section 2.1 will present the experimental setup and section 2.3 will deal with the fact that our coil is finite.

This new novel technique is used to determine ρ_s and J_c or ξ without any leads or magnetic field. Another advantage of this technique is that it demands a global phase coherence. Therefore, phase transitions are much sharper compared to other techniques such as transport measurement or magnetization measurement of the Meissner Effect.

2.1 Experimental Setup

The coil we used for stiffness measurements near T_c is 60 mm long and its external diameter is 0.8 mm. It is made of copper wire and has two layers and 1214 winding in total. For the critical current measurements in low temperatures, we used a different coil. The coil was also 60 mm long, but its external diameter was 0.98 mm and had four layers and 2400 winding in total. It was made of NbTi SC wire, allowing us to reach a current of more than 10 Amp. The coil goes through the hole of the ring-shaped sample and

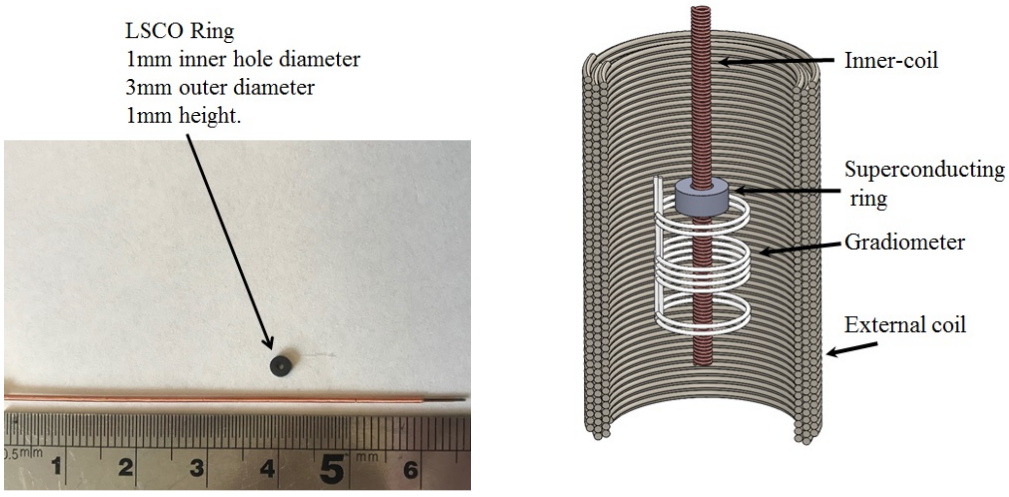

(a) (b)

Figure 2.1: (a) Ring-shaped sample and a 60 mm long copper coil. (b) Illustration of the long coil with the ring on it, the Gradiometer and the External Coil.

the ring is in its center. The pickup loop is actually a Gradiometer combined of 8 loops and it is static, while the coil and the rings are going up and down through it. A seconds external coil, is used to cancel external magnetic fields stronger than 0.001 Oe. The gradiometer is connected to a SQUID that measures the magnetic flux of both the ring and the coil and because of the gradiometer's geometry the output signal of the SQUID has a unique shape. Explanation on the gradiometer's signal will be given in App A.1 and explanation on the gradiometer's signal will be given in Sec 2.2. In Fig 2.1a, one can see the ring-shaped sample and the 60 mm long copper coil. Figure 2.1b shows the long excitation coil with the ring on it, the gradiometer and the external coil.

During the measurements, the ring is fixed at the center of the coil and together they move along the z direction (the x-axis in the graph), in and out of the gradiometer which is fixed at $z = 0$. When they move, the magnetic flux through the gradiometer is changing, the SQUID measures the change and we see it as output voltage. Figure 2.2 presents such measurements of a LSCO ring above and below T_c. By measuring the coil without the ring or by measuring above T_c, we are able to get the coil's signal. By subtracting the coil's signal from the combined signal, we get the ring's signal. The difference between the maximum and the minimum of the ring's signal is called ΔV_{ring} and the difference between the maximum and the minimum of the coil's signal is called ΔV_{coil}. The measurable parameters ΔV_{ring} and ΔV_{coil} are proportional to the magnetic flux generated by the ring and coil respectively.

2.2 SQUID Magnetometer

Based on the Josephson junction effect (JJE), the superconducting quantum interference device (SQUID) is commonly used to detect magnetic moment. We used a S600 SQUID SUSCEPTOMETER of CRYOGENIC LTD. The SQUID's output is in voltage and proportional to the magnetic flux through the gradiometer. The output voltage of our device can be translated to units of magnetic moment with resolution of $1 \cdot 10^{-9}\,\mathrm{Am}^2$.

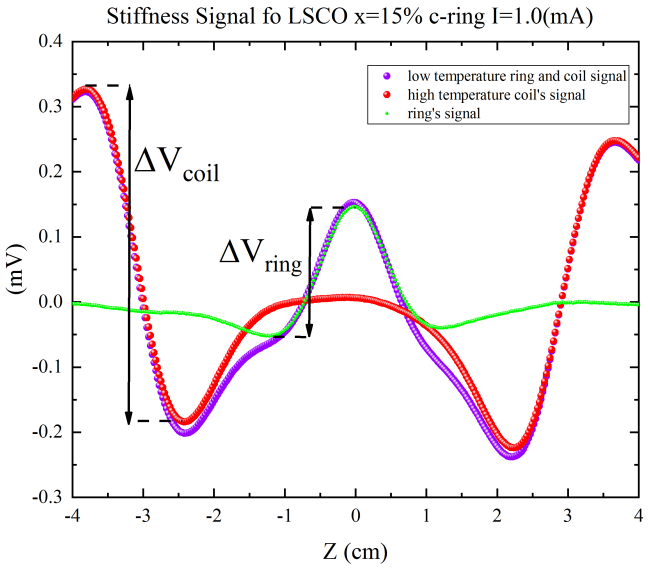

Figure 2.2: Stiffness measurements of OPD LSCO ring with current of 1.0 (mAmp). During the measurements, the ring and coil are moving along the z direction (the x-axis in the graph), in and out of the gradiometer which is fixed at $z = 0$. When they move, the magnetic flux through the gradiometer is changing, the SQUID measures the change and we get the output voltage (y-axis in the graph). The measurements below T_c are in purple and show the combined signal of the ring (the sample) and the coil. The measurements above T_c are in red and show only the coil's signal because the ring is no longer superconducting. By subtracting the coil signal from the combined signal we get the ring's signal, shown in green. The difference between the maximum and the minimum of the ring's signal is called ΔV_{ring} and the difference between the maximum and the minimum of the coil's signal is called ΔV_{coil}.

2.3 Verification

To check this new technique, instead of following the regular ZGFC protocol, we tried a different protocol. We started by turning on the current in the coil when the sample was above T_c and only then cooling the sample below T_c (unlike the usual processes of cooling before turning on the current in the coil). We call this process Gauge-Field-Cooling (GFC). Below T_c the sample is superconducting and should react to any magnetic field, but the only signal we measured after GFC was the coil's signal. When we turned off the current in the coil and measured again, the coil signal vanished, but we got the ring's signal which was identical to to ring's signal we got after subtracting the coil's signal from the combined signal in the regular ZGFC process. Those results strongly support our assumption that the difference between our long coil and an infinite-coil is minor and legitimize our technique.

To explain those results, we need to look back at Eq 1.1. When we follow the GFC protocol, $\boldsymbol{A} \neq 0$ when cooling, and the SC will choose $\nabla\varphi \neq 0$ so that $\boldsymbol{J}_s$ will be as small as possible ($\boldsymbol{\nabla}\varphi$ is constrained because for any closed loop of radios r, $\boldsymbol{\nabla}\varphi$ must be equal to: $\frac{l}{r}\hat{\varphi}$ where l is an integer) to minimize the free energy. And when the current is turned off, $\boldsymbol{A} = \boldsymbol{0}$ but φ again doesn't change, and we get $\boldsymbol{J}_s = \hat{\rho}_s \frac{\hbar c}{q} \boldsymbol{\nabla}\varphi \neq 0$.

Figure 2.3 shows the results of the GFC experiment. We also checked whether the GFC protocol will give different results when we change the temperature, but no difference was found in comparison with the ZGFC protocol, as can be seen in the inset of Fig 2.3. The GFC protocol was used

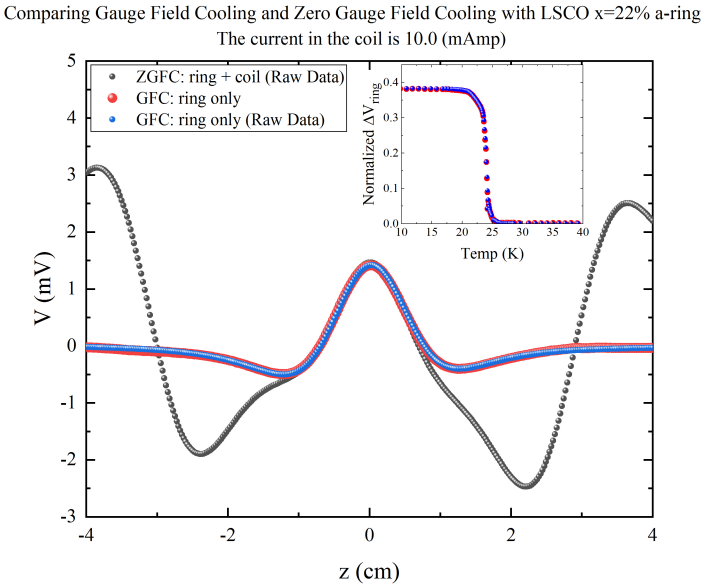

Figure 2.3: Raw signal of Gauge-Field-Cooling (GFC), and Zero-Gauge-Field-Cooling (ZGFC) measurements after subtracting the coil's signal. The inset shows stiffness measurements of the two protocols. Both in the raw signal and the stiffness measurements, the two different protocols give the same results.

only for this verification, and ZGFC was used for all the measurements in this work.

2.4 Stiffnessometer Theory

Before we find the stiffness or the critical current, we need to deal with the fact that $\boldsymbol{J}_s$ is not equally distributed inside the ring and it might reach its critical value in one place before another. Also, the relevant vector potential in Eq 1.2 $\boldsymbol{A}$ is the total vector potential with contribution from the vector

potential produced by the coil $\boldsymbol{A}_{coil}$ and the vector potential generated by the ring $\boldsymbol{A}_{ring}$. Now equation 1.2 looks different:

$$\boldsymbol{J}_s = -\hat{\rho_s}\boldsymbol{A}_{tot} = -\frac{1}{\mu_0\lambda^2}(\boldsymbol{A}_{coil} + \boldsymbol{A}_{ring}). \tag{2.1}$$

By using Maxwell's equation: $\boldsymbol{J} = \frac{1}{\mu_0}\boldsymbol{\nabla} \times \boldsymbol{\nabla} \times \boldsymbol{A} = -\frac{1}{\mu_0}\boldsymbol{\nabla^2 A}$ (using the coulomb gauge), we get a partial differential equation (PDE for $\boldsymbol{A}_{ring}$:

$$\boldsymbol{\nabla}^2\boldsymbol{A}_{ring} = \frac{1}{\lambda^2}(\boldsymbol{A}_{coil} + \boldsymbol{A}_{ring}). \tag{2.2}$$

The magnetic flux of the coil through a single pickup loop is: $\Phi_{coil} = \int \boldsymbol{B} \cdot d\,\boldsymbol{a} = \oint \boldsymbol{A} \cdot d\boldsymbol{l} = \boldsymbol{2\pi}\mu_0 nI$ and we can write 2.2 as: $\boldsymbol{\nabla}^2\boldsymbol{A}_{ring} = \frac{1}{\lambda^2}(\frac{\Phi_{coil}}{2\pi r}\hat{\varphi} + \boldsymbol{A}_{ring})$ where $\hat{\varphi}$ is the azimuthal direction. We switch to unit-less parameters by defining:

$$r/R_{PL}{\rightarrow}r, A_{ring}/A_{coil}(R_{PL}){\rightarrow}A, \lambda/r_{PL}{\rightarrow}\lambda, z/R_{PL}{\rightarrow}z \tag{2.3}$$

Using cylindrical coordinates and the symmetry of the system ($\boldsymbol{A} = A(r,z)\hat{\varphi}$) we get a unit-less PDE:

$$\frac{\partial^2 A}{\partial z^2} + \frac{\partial^2 A}{\partial r^2} + \frac{1}{r}\frac{\partial A}{\partial r} - \frac{A}{r^2} = \frac{1}{\lambda^2}(A + \frac{1}{r}) \tag{2.4}$$

where A is a unit-less vector potential in the azimuthal direction ($\hat{\varphi}$). r and λ in this equation are also unit-less. We solved this PDE numerically

with the following boundary conditions (BC): $A(r=0,z) = A(r \to \infty, z) = A(r, z \to \pm\infty) = 0$, and taking λ to infinity outside of the ring. We used $FreeFem++$ and also confirmed the solution with $Comsol\,5.3a$ (calculated by Nir Gavish).

2.5 Stiffness Measurements

To measure the stiffness, we look at the ratio between the ring's vector potential and the coil's vector potential at the pickup-loop. Those vector potentials are proportional to the magnetic flux through the pickup-loop created by the ring or coil and so we can find a relation between the SQUID's signal and the vector potential. The ring's signal will be ΔV_{ring} and the coil signal will be ΔV_{coil}. Both are explained in section 2.1 and presented in Fig 2.2. Since we use a ring-shaped sample and a gradiometer, there is a geometrical factor we call "G" that defines the relation between the calculation done for a single pickup loop and the results of measuring with the gradiometer. G can be found experimentally (calibration) by comparing between the saturation value of the numerical calculation for $\lambda \to 0$ (presented in Fig 2.4) and the measured saturation at low temperatures, where λ is very small. The relation is: $\frac{\Delta V_{ring}}{\Delta V_{coil}} = G\frac{A_{ring}(r_{pl})}{A_{coil}(r_{pl})}$. Another way to determine G is by a calculation shown in App A.1. The proportionality constant between the output voltage and the vector potential is irrelevant, because we look at the ratios.

Solving the PDE 2.4 for many different λ's, we can plot the ratio between the vector potentials of the coil and the ring at $r = r_{pl}$ as func-

tion of λ as shown in Fig 2.4. We convert the measured $\Delta V_{ring}/\Delta V_{coil}$ to $A_{ring}(r_{pl})/A_{coil}(r_{pl})$ using G, and obtain λ or the stiffness ρ_s from the graph. But since for very small λ, or very large λ, the numerical solution saturates, small changes in $\Delta V_{ring}/\Delta V_{coil}$ leads to big changes in λ. So our method is good only for $0.1 \leq \lambda \leq 3\,\text{mm}$. At low temperatures, λ is too small for our technique, but close to T_c, λ gets bigger and we can measure it where no other technique can.

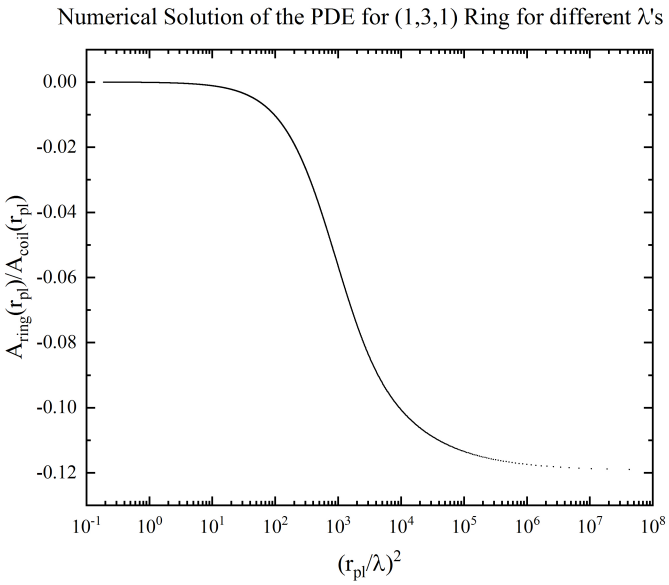

Figure 2.4: Numerical solution of the PDE Eq 2.4 for different λ's. $r_{pl} = 13\,\text{mm}$ is the radius of the pickup loop. This numerical solution depends on the ring's measures (ID $= 1.0\,\text{mm}$, OD $= 3.0\,\text{mm}$, H $= 1.0\,\text{mm}$).

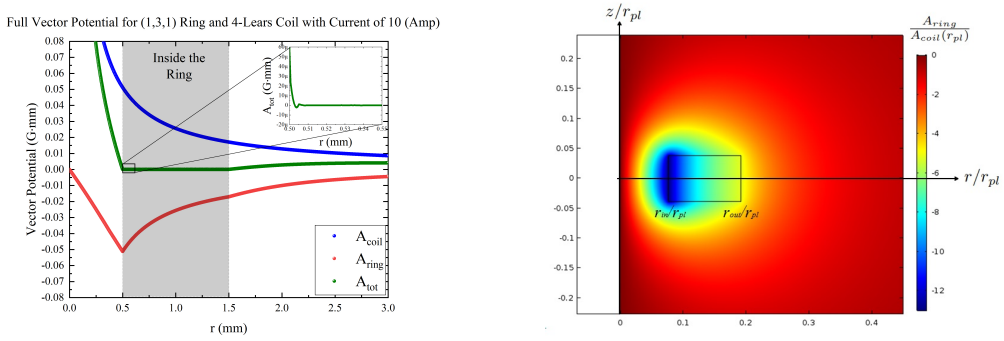

(a) (b)

Figure 2.5: (a) The total vector potential as function of r at $z = 0$ presented in green. the ring's and the coil's vector potential are presented as well in red and blue. The inset shows a closer look at the inner edge of the ring. (b) The numerical solution of the unite less PDE Eq 2.4 with BC $A(r = 0, z) = A(r \to \infty, z) = A(r, z \to \pm\infty) = 0$, in the $r - z$ plan. The ring's dimensions are: ID $-$ 1.0 mm, OD $-$ 3.0 mm and height $-$ 1.0 mm. $\lambda = 300$ nm. The colors represent the intensity of the unite less ring's vector potential.

2.6 Critical Vector-Potential Measurements

Staying stable at the same temperature, we can increase the current through the coil until the linear behavior between the current and the signal breaks. When this happens, the linearity between $\boldsymbol{A}$ and $\boldsymbol{J}_s$ breaks and we know we have reached the critical vector potential A^c which can be interpreted as critical velocity v_c, critical current J_c or coherence length ξ, of the sample.

Figure 2.5b shows the numerical solution of Eq 2.4 in the $r - z$ plan. In reality, the ring's dimensions are: Inner Diameter (ID) 1.0 mm, Outer Diameter (OD) 3.0 mm, and height 1.0 mm. The penetration depth was taken to be $\lambda = 300$ nm (λ is chosen from *low energy* μsr measurements of

LSCO at low temperatures [2]). When measuring the critical current at low temperatures, we must take λ from outer source because at low temperatures our stiffnessometer is not accurate enough. The colors represent the intensity of the unit-less ring's vector potential. In Figure 2.5a we see the total vector potential inside the ring where $\boldsymbol{A}_{coil} = \mu_0 \frac{In}{r}\hat{\varphi}$ and $\boldsymbol{A}_{ring} = A \cdot A_{coil}(R_{pl})\hat{\varphi}$ where A comes from the numerical solution and $A_{coil}(R_{pl})$ is the coil's vector potential at the radios of the pickup-loop. The inset of Fig 2.5a shows A_{tot} near the inner radius of the ring where it is the most intense. It should be pointed out, that the coil we actually use is finite and the relation $\boldsymbol{A}_{coil} = \frac{\mu_0 In}{r}\hat{\varphi}$ is an approximation. We will deal with this finite-coil-issue in section 2.3.

To calculate the critical velocity, we can look at the right part of Eq 1.7 and get:

$$v_c = \frac{e^* A^c_{tot}(R_{in})}{m^* c}. \tag{2.5}$$

where $A^c_{tot}(R_{in})$ is the critical A_{tot} in the inner radius of the ring. This is called the PDE solution method. From Eq 1.14 $\xi = \frac{\hbar}{\sqrt{3}m^* v_c}$ we find ξ and also from Eq 1.15 $J_c = \frac{m_e c^2}{6\pi e \lambda^2} v_c$ we find J_c. But, there is a problem with this technique. Due to the exponential behavior of the total vector potential at inner radius of the ring (as can be seen in the inset of Fig 2.5a), small errors in R_{in} leads to big errors in ξ. So we must think of something else.

The approximated method is based on the fact that when looking at the inset of Fig 2.5a it is clear that the vector potential and so the currents,

exist only on the inner radius of the ring. We can think of another much simpler way to calculate J_c. It is done by thinking about the super currents density of the ring as if they run inside a cylinder surrounding the inner coil and canceling its magnetic field. Imagine Ampere's loop as a square with one limp of length l along the z-axis in the center of the ring and the coil where the ring's field and the coil's field cancels each other and another limp of length l inside the ring (and out side of the coil) were the magnetic field is also zero. The two other limps will be perpendicular to the z-axis. Now, we can use Ampere's law: $\oint B \cdot dl = \mu_0 I_{enclosed}$. The left side will be $\oint B = l \cdot (B_{coil} - B_{ring}) = 0$ and the right side $\mu_0 I_{enclosed} = \mu_0 l(nI_{coil} - I_{ring})$. We will take the current density to be $J_s(r) = J_c e^{-(r-r_{in})/\lambda}$ and then $I_{ring} = \int_{r_{in}}^{r_{out}} J_s(r) \cdot dr = J_c\lambda(1 - e^{-(r_{out}-r_{in})/\lambda}) \approx J_c\lambda$. Thus

$$J_c = nI_c/\lambda.$$

3 Results

3.1 Stiffness Measurements Results

Figure 2.5a presents stiffness measurements of a and c rings of LSCO $x = 17\,\%$ as function of the temperature for different currents. All other data sets are given in appendix A.2. As can be seen, the a-ring transition start at different temperature, but ends at the same temperature for all currents. The c-ring start and finish the transition at the same temperatures for all currents. It is clear that the two rings have two different critical temperatures although they are made from the same single crystal. This critical temperature difference is what we call ΔT_c, and T_c is define as the temperature where the stiffness is zero (this point is the same for all currents of both rings). We repeat these measurements for different crystals of different doping to examine the variations of ΔT_c with doping. We also did critical current measurements for each ring as close as we could to T_c, which can be seen in the inset of Fig 2.5a. Those measurements were done at fixed temperatures, marked with black arrows pointing on the transition at the main graph. The critical current from those measurements is about 1.0 mAmp. It was a difficult measurement to preform, because close to T_c, any small instability of the temperature could have influenced the measurements.

In Fig 2.5b one can see magnetization measurements of the two rings. Each ring was measured in two different orientations, one time "standing" with the symmetry axis of the ring perpendicular to the magnetic field (the

magnetic field is parallel with the rings plane) and one time "laying", with the symmetry axis of the ring parallel to the magnetic field (the magnetic field is perpendicular with the rings plane).

When a ring is standing, the field doesn't go through the hole, and both rings have similar phase transition in this position. But, the standing a-ring mid-transition is at a slightly higher temperature. This happens because when the a-ring is standing the copper-oxide planes are perpendicular to the magnetic field and for the standing c-ring the copper-oxide planes are now parallel with the magnetic field. When a ring is laying, the magnetic field goes through the hole and the measured moment corresponds to both the change of flux through the hole and the expulsion of the field from the SC bulk (due to the Meissner effect). The expulsion from the bulk can be microscopic or macroscopic phenomena, but the reaction to the change of flux through the hole must be macroscopic. We suspect that this is the reason why the laying a-ring transition has two parts. But, we don't see any sign of such behavior with the laying c-ring. This two-parts transition was observed in the magnetization measurements of all laying a-rings, but in none of the c-rings. It is possible that vertices can move easily between the CuO_2 planes and because the laying a-ring have weak parts where vortices can move in or out from the hole of the ring without crossing the planes, we see the two-part transition.

The mid-transition of the laying c-ring is closer in temperature to the standing a-ring's mid-transition because, in both of those cases the copper-

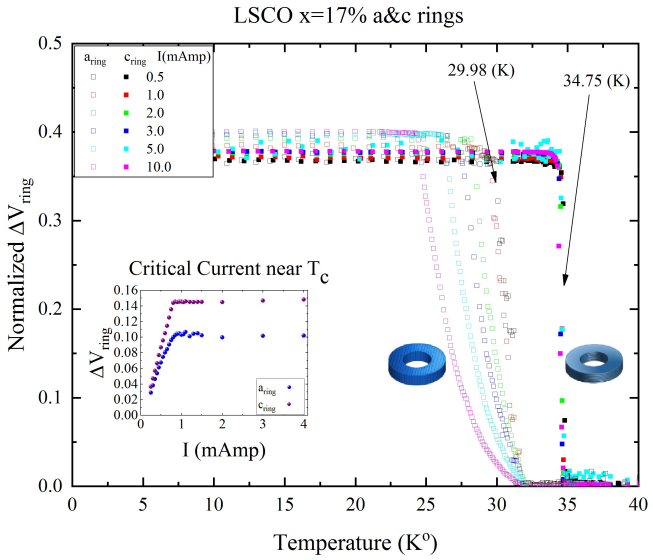

Figure 3.1: Stiffness measurements of a and c rings of LSCO $x = 17\,\%$ as function of the temperature for different currents. The full marks belong to the c-ring and the hollow marks belong to the a-ring. The x-axis is the temperature in K, and the y-axis is the normalized ΔV_{ring} which equals to $\Delta V_{ring}/\Delta V_{coil}$. The inset shows critical-current measurements at the transition temperature for both rings with the c-ring's measurements in purple and the a-ring's in blue. The critical measurements were done at fixed temperatures close to T_c, and marked with black arrows on the main graph.

oxide planes are perpendicular with the magnetic field. In the stiffnessometer, we only see the macroscopic phenomena and the difference in T_c are much more clear. This magnetization measurement also assures us that the T_c difference we see in the stiffness measurements are not the artifact of some en-homogeneous doping of the single crystal we used to cut our rings from.

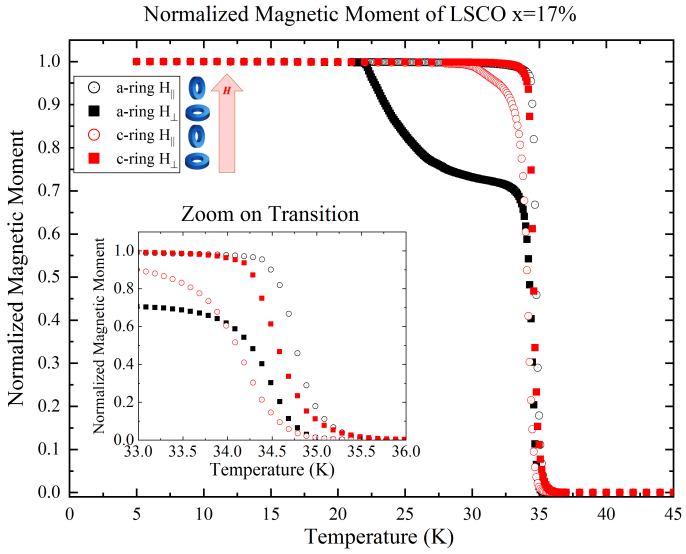

Figure 3.2: Normalized magnetic moment measurements of a and c rings of LSCO $x = 17\,\%$ for different temperature with field of $H \approx 2.0\,\mathrm{Oe}$. There are two measurements for each ring: one with the magnetic field parallel to the ring and the other with perpendicular field. The inset is a zoom-in on the transition.

3.2 Critical Current Measurements Results

In Fig 3.3 one can see two sets of measurements of two different rings made from the same crystal of LSCO with doping of 22 % which is in the OVD regime. Both measurements were done with the same SC excitation coil with 4 winding layers (2400 windings in total) at 1.7 K well below the T_c of the samples. The rings parameters were: ID-1.0 mm, OD-3.0 mm and height-1.0 mm. One sample is a c-ring (current flow in the CuO_2 planes) and the other sample is an a-ring (current flow in and between the CuO_2 planes). The a-ring breaks from linearity at about 6 Amp while the c-ring's signal stays linear all the way up to 10 Amp.

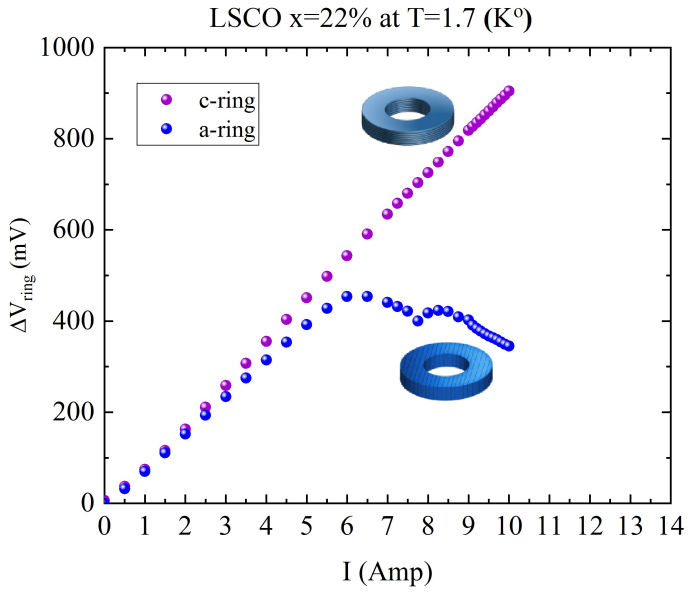

Figure 3.3: Critical-Current measurements of a and c rings from the same OVD LSCO single crystal $x = 22\,\%$. The temperature during the measurement was 1.7 K and the coil was a superconducting coil with four layers of winding (2400 windings in total). The y-axis is $\Delta V_{ring}$and the x-axis is the current in the coil.

4 Data Analysis and Discussion

The two main results of this thesis are: I) ξ measurements of LSCO SC at $T \to 0$. II) The construction of a phase diagram of the critical temperature difference between in-plane and out-of plane stiffness as function of hole doping x.

4.1 Penetration Depth λ

When stiffness measurements are done for c-ring we can translate them to the out-of-plane penetration depth λ_{ab} following the steps explained in 2.5. From measurements of the a-ring, we can only extract an effective penetration depth λ_{eff} because the PDE is for azimuthal-symmetric system unlike the a-ring. Figure 4.1 show λ_{ab} and λ_{eff} for $x = 17\,\%$ LSCO. The red arrows mark the temperature where critical current measurements were done.

4.2 Stiffness Behavior near T_c

Figure 4.2 presents λ^{-2} (proportional to $\hat{\rho}_s$) as function of temperature for four different doping. The red lines are guide-to-the-eye, marking the trend of the stiffness. At $x = 12.5\,\%$, the lines diverge when the temperature is increased, at $x = 15\,\%$ they look like they are perpendicular and for $x = 17\,\%$ the lines converge. At $20\,\%$ the lines also converge with increasing temperature but not as fast as the $17\,\%$. This dome like behavior of the stiffness trend with doping is noticeable also with T_c and ΔT_c (but the T_c

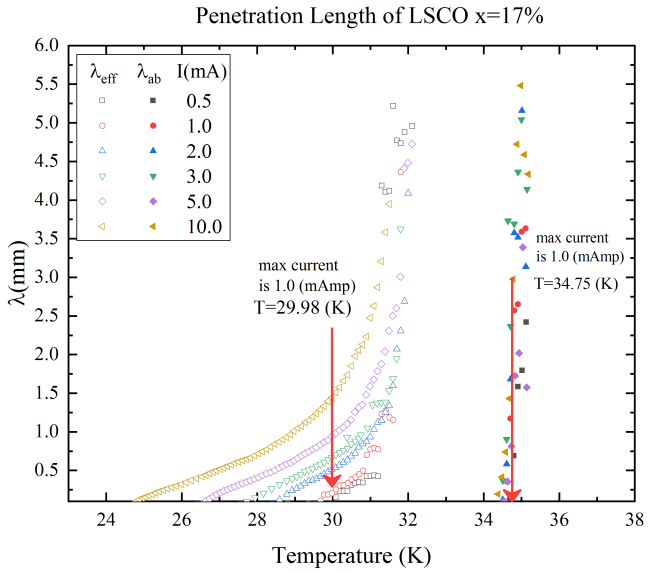

Figure 4.1: Penetration depth λ_{ab} (full marks) and effective penetration depth $\lambda_{effective}$ (hollow marks) for LSCO $x = 17\,\%$ as function of temperature calculated from stiffness measurements with different currents in the coil (different colors), and a numerical solution of the PDE. The red arrows mark the temperature at which the critical current measurements where done.

maximum is at 15 % and not 17 %). If we extrapolate the red lines (linearly) to see at what temperature they meet for each doping, we see that at 15 %, the lines meet only above 45 K (above the highest possible T_c for LSCO), at 17 % they meet at $\backsim$ 38 K and at 20 % at $\backsim$ 33 K, and the $x = 12.5\,\%$ aren't going to meet at all.

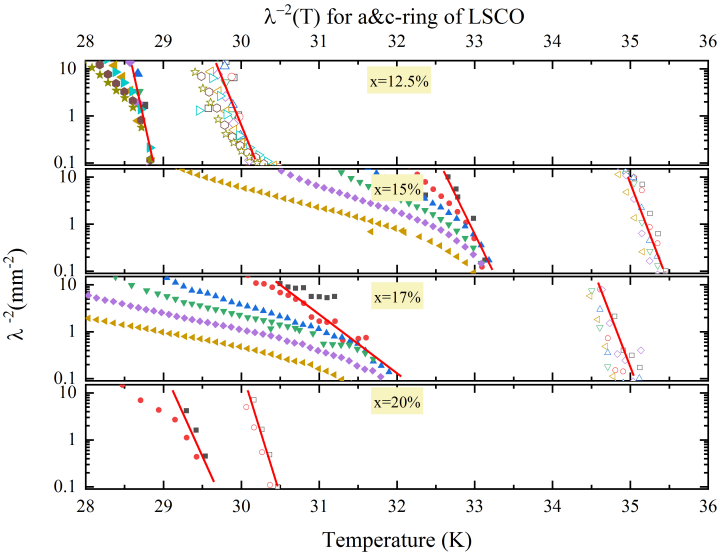

Figure 4.2: Logarithmic plot of λ^{-2} as function of temperature for a and c rings of LSCO 17 % calculated from stiffness measurements with different currents in the coil (different colors), and a numerical solution of the PDE. Full marks are used for the c-ring and hollow marks for the a-ring. The red lines are guide-to-the-eye marking the trend of the stiffness.

4.3 LSCO Phase Diagram of ΔT_c and Doping

Figure 4.3 shows the critical temperature of both a and c-rings and ΔT_c for LSCO of different doping. As can be seen, ΔT_c is always positive except for the 11 %. In the far OVD and far UND regimes ΔT_c goes up, but between 11 % and 20 % a dome-like structure is formed.

Our findings from stiffness measurements of a-type and c-type LSCO rings shows a clear an-isotropic behavior. The fact that the c-ring have higher T_c than the a-ring of the same doping for all doping except for the $x = 11\,\%$, matches our assumption that SC is stronger within the copper-oxide

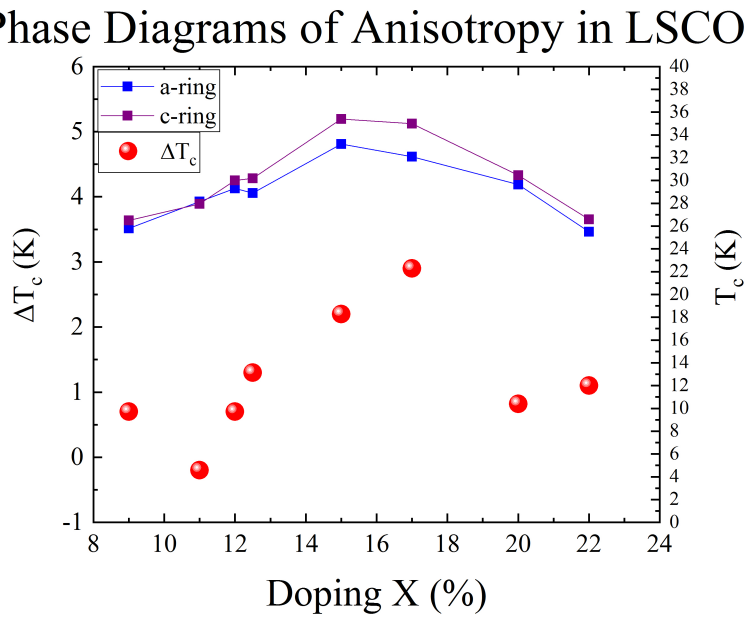

Figure 4.3: LSCO phase diagram. Red spheres mark ΔT_c (the left y-axis) as function of Sr doping (the x-axis). Blue and purple marks belong to T_c (the right y-axis) of a and c rings respectively also as function of Sr doping (the x-axis).

planes. The magnetic moment measurements denies doping in-homogeneity as the cause for ΔT_c. The critical current measurements near the transition indicate how far our stiffness analysis is valid with certainty. The the fact that when we increase the current, the transition ends at the same temperature indicates a lack of current dependence of the critical temperature. The dome like behavior of ΔT_c was an interesting discovery and the sharp decrease around the critical doping $x = 19\,\%$ rise questions about the relation between anisotropy and the quantum critical point.

4.4 Coherence Length

The different behavior in Fig 3.3 between the two samples imply that superconductivity is much "stronger" in-plane than out-of-plane. The a-ring is not rotationaly symmetric, so our assumptions and the solution of the PDE 2.4 is not valid in this case and we cannot extract v_c or the between-plane coherence length ξ_c from this measurement (yet). The c-ring is rotationaly symmetric and although we did not reach the break point, we now know it must be above 10 Amp. So, the critical velocity must be bigger than the velocity at 10 Amp and the in-plane coherence length ξ_{ab} must be smaller than we would calculate for this velocity. We can set a lower limit on the critical velocity and an upper limit on the coherence length. For OVD LSCO $x = 22\,\%$ at 1.7 K and taking λ to be 300 nm (λ is chosen based on *low energy* μsr measurements of LSCO at low temperatures [2]) and using the PDE solution method, we see that v_c is bigger than $8.35 \cdot 10^3$ m/s and ξ_{ab} is smaller than 4 nm. J_c will be bigger than $2.8 \cdot 10^7$ Amp/cm^2.

Using the approximated method for $I_{coil} = 10$ Amp, $n = 400\,\text{cm}^{-1}$ and $\lambda = 3 \cdot 10^{-5}$ cm, we get: $J_c > 1.3 \cdot 10^8$ Amp/cm^2. Then, by using Eq 1.16 and Eq 1.14 we see that $v_c > 3.88 \cdot 10^4$ m/s and $\xi < 0.86$ nm. This ξ is on the order of one unit cell (~ 3.78 Å). The results of the approximated method are different by factor of 5 from the PDE solution method.

We can compere our results with Fermi velocity calculated from the dispersion relation of the nodal-direction: $v_f \approx \frac{2\,\text{eVÅ}}{\hbar} \approx 3 \cdot 10^5$ m/s (taken from [10]). Our lower limits on the critical velocity are much smaller than

Fermi velocity.

Let's compere our results to the BCS prediction for the depairing-velocity and SC gap energy of $\Delta \sim 10\,\mathrm{meV}$ (from measurements of OVD LSCO $x = 21\,\%$ by [11] using STM). $v_d^{BCS} = \frac{\Delta}{\hbar k_f} \approx 1.8 \cdot 10^3\,\mathrm{m/s}$ where k_f is the Fermi wave vector and in our case, $k_f = \frac{\pi}{a} \approx 8.3 \cdot 10^9\,m^{-1}$. This v_d^{BCS} is smaller than our lower limit of both methods.

Although the technique is not (yet) perfect, we get good results of the same order of magnitude from both options and the main principle of the Stiffnessometer works. The early break from linearity of the a-ring compared with the c-ring is exactly what we expected and shows the potential of this method. A more conventional way of measuring ξ is by measuring the second critical field H_{c2} and use the relation $\xi = \sqrt{\Phi_0/2\pi H_{c2}}$. For $\xi = 2\,\mathrm{nm}$, one needs to reach fields of about 100 T. We intend to reach the same results at equilibrium and with less effort.

5 Concluding Remarks

In this work we presented the Stiffnessometer and the way it can be used to measure the stiffness near T_c and extract λ, or measuring the critical vector potential and extract the critical velocity and ξ. The critical current measurements of the OVD LSCO $x = 22\,\%$ showed an-isotropic behavior when the a-ring broke from the linear dependence at 6 Amp, while the c-ring stayed linear up to 10 Amp. We proposed two ways to extract the critical velocity and ξ. Both gave results of the same order of magnitude and by comparing to Fermi velocity our critical velocity limits were more than order of magnitude smaller. The BCS depairing velocity calculated for $\Delta \sim 10\,\mathrm{meV}$ was smaller than the lower limit of both methods. In the future we intend to increase the total vector potential and improve our data analyses to manage precise ξ measurements at low temperatures for all doping.

The stiffness measurements near T_c revealed a dome-like behavior of ΔT_c, starting at $x = 11\,\%$ near the 1/8 doping and ended at $x = 20\,\%$ close to the quantum critical point. The maximum ΔT_c is $2.9\,\mathrm{K}$ at $x = 17\,\%$ near the OPD. Those findings rises questions abut possible relations between this an-isotropic dependence of ΔT_c to other phenomena such as the opening of the pseudogap or the phase transition between strange metal and Fermi liquid.

A Appendix

A.1 Gradiometer

The SQUID signal is proportional to the total magnetic flux that goes through the gradiometer which is the sum of the flux through each one of the eight pickup loops of the gradiometer. Those loops are arranged so that four loops are in the center of the gradiometer with the same orientation, and the other four loops are split into two pairs. One pair is set 7 mm above the center of the gradiometer and the other pair is 7 mm below. The four external loops (the two pairs) have different orientation then the four loops in the center. The total flux will be: $\Phi_{tot} = -2\Phi(z-7) + 4\Phi(z) - 2\Phi(z+7)$, where z is the location of the sample relative to the center of the gradiometer (the flux Φ depends on the distance between the sample and the loop). In some way Φ_{tot} reminds a second derivative of the total magnetic flux in the center of the gradiometer. When measuring the ring, the magnetic flux depends on the vector potential of the ring which depends on its distance from the loop's center (z) as: $A_{ring}(z) = 2\pi m r_{pl}^2/(r_{pl}^2 + z^2)^{\frac{3}{2}}$, where m is the ring's magnetic moment. The ratio between vector potential on a gradiometer and vector potential on a single pickup loop at $z = 0$ is: $\frac{A_{ring}^{gradiometer}(z)}{A_{ring}^{pickup-loop}(z=0)} = \frac{-2r_{pl}^3}{(r_{pl}^2+(z+7)^2)^{\frac{3}{2}}} + \frac{+4r_{pl}^3}{(r_{pl}^2+z^2)^{\frac{3}{2}}} + \frac{-2r_{pl}^3}{(r_{pl}^2+(z-7)^2)^{\frac{3}{2}}}$. The difference between the maximum and minimum of this function is: $\frac{\Delta A_{ring}^{gradiometer}}{A_{ring}^{pickup-loop}(z=0)} = 1.7$. Doing the same process for our finite 60 mm long coil we get $\frac{\Delta A_{coil}^{gradiometer}}{A_{coil}^{pickup-loop}(z=0)} = 0.47$. The Voltage output is proportional to the sum of the flux through all eight pickup loops:

$V_{output}(z) = K \cdot \Sigma_{all-pl} \int \boldsymbol{B}(z - z_{pl}) \cdot d\boldsymbol{a} = K \cdot \Sigma_{all-pl} \int A(z - z_{pl}) \cdot dl = K \cdot 2\pi r_{pl} A^{gradiometer}(r_{pl}, z)$ where K is some constant ($V_{output} = K \cdot \Phi_{pickup-loop}$). We expect that: $\frac{\Delta V_{ring}}{\Delta V_{coil}} = 3.62 \frac{A_{ring}^{pickup-loop}(z=0)}{A_{coil}^{pickup-loop}(z=0)}$. We can compere this result to the experimental way of getting G explained in Sec 2.5. The saturation value of $\frac{\Delta V_{ring}}{\Delta V_{coil}}$ for low temperatures in Fig. 3.1 for the c-ring of LSCO 17 % is about 0.37 and for big λ we get $\frac{A_{ring}^{pickup-loop}}{A_{coil}^{pickup-loop}} = -0.105$ from the numerical solution of the PDE for the ring we measured (ID = 1.0 mm,OD = 2.48 mm,hight = 1.0 mm) . The experimental G we get is: $0.37/0.105 \approx 3.52$ not so far from our calculation of G. For the calculation of λ we used the experimental G which is different for each ring depending on its geometry.

A.2 Stiffness Measurements for Different Doping

We did several stiffness measurements of a and c rings of different doping from 9 % to 22 %. In all those measurements, we cooled the system to 5 K with $\boldsymbol{A} = 0$ (ZGFC protocol), turned on the current in the excitation coil and measured the magnetization at different temperatures. All those measurements are presented in the following figures: (Fig A.1, and Fig A.2).

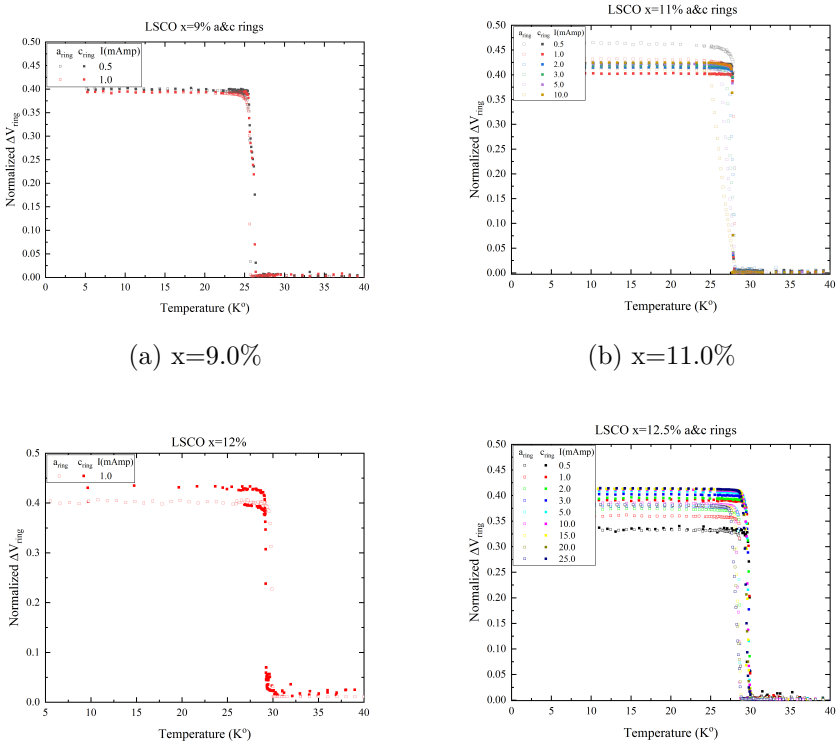

(a) x=9.0%

(b) x=11.0%

(c) x=12.0%

(d) x=12.5%

Figure A.1: Stiffness Measurements for Different Doping (UND)

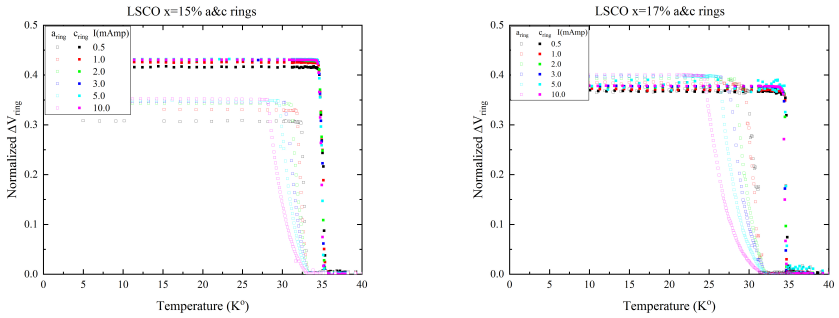

(a) x=15.0% (b) x=17.0%

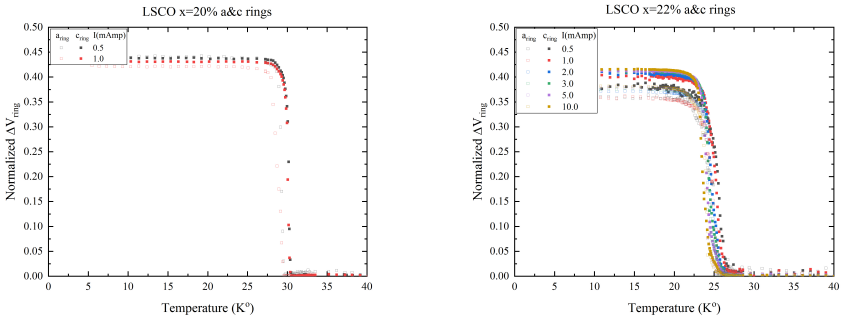

(c) x=20.0% (d) x=22.0%

Figure A.2: Stiffness Measurements for Different Doping (OVD)

References

[1] I. Kapon, "Stiffnessometer, a magnetic-field-free superconducting stiffness meter and its application," in *Springer Theses* (Springer International Publishing, 2019) pp. 19–33.

[2] I. Kapon, Z. Salman, I. Mangel, T. Prokscha, N. Gavish, and A. Keren, "Phase transition in the cuprates from a magnetic-field-free stiffness meter viewpoint," Nat. Commun. **10**, (2019).

[3] X. Y. Tee, T. Ito, T. Ushiyama, Y. Tomioka, I. Martin, and C. Panagopoulos, "Two superconducting transitions in single-crystal $La_{2-x}Ba_xCuO_4$," Phys. Rev. B **95**, (2017).

[4] G. Drachuck, M. Shay, G. Bazalitsky, J. Berger, and A. Keren, "Parallel and perpendicular susceptibility above T_c in $La_{2-x}Sr_xCuO_4$ single crystals," Phys. Rev. B **85**, (2012).

[5] M. Tinkham, *Introduction to Superconductivity: v. 1* (Dover Publications Inc., 2004).

[6] P. Giraldo-Gallo, J. A. Galvis, Z. Stegen, K. A. Modic, F. F. Balakirev, J. B. Betts, X. Lian, C. Moir, S. C. Riggs, J. Wu, A. T. Bollinger, X. He, I. Božović, B. J. Ramshaw, R. D. McDonald, G. S. Boebinger, and A. Shekhter, "Scale-invariant magnetoresistance in a cuprate superconductor," Science **361**, 479–481 (2018).

[7] A. Damascelli, Z. Hussain, and Z.-X. Shen, "Angle-resolved photoemission studies of the cuprate superconductors," Rev. Mod. Phys. **75**, 473–541 (2003).

[8] B. Keimer, S. A. Kivelson, M. R. Norman, S. Uchida, and J. Zaanen, "From quantum matter to high-temperature superconductivity in copper oxides," Nature **518**, 179–186 (2015).

[9] S. M. Koohpayeh, D. Fort, and J. S. Abell, "The optical floating zone technique: A review of experimental procedures with special reference to oxides," Prog. Cryst. Growth Charact. Mater. **54**, 121–137 (2008).

[10] B. Edegger, V. N. Muthukumar, C. Gros, and P. W. Anderson, "Electronic structure of strongly correlatedd-wave superconductors," Phys. Rev. Lett. **96**, (2006).

[11] T. Kato, T. Maruyama, S. Okitsu, and H. Sakata, "Doping dependence of two energy scales in the tunneling spectra of superconducting la2-xSrxCuO4," J. Phys. Soc. Jpn. **77**, 054710 (2008).

את התוצאות של כל מדידות הקשיחות ריכזנו ביחד ליצירת דיאגרמת פאזות חדשה עבור LSCO המציגה את ההפרש בין הטמפרטורה הקריטית שנמדדה עבור טבעת־c לטמפרטורה הקריטית שנמדדה עבור טבעת־a, עבור רמות אילוח שונות. להפרש בין הטמפרטורות הקריטיות אני קוראים ΔT_c. מצאנו כי עבור כל רמות האילוח השונות שמדדנו מלבת אחת (שבה ΔT_c הינו אפסי), הטמפרטורות הקריטית של טבעת־c תמיד גדולה מזו של טבעת־a. בין רמת אילוח של $11\,\%$ לרמת אילוח של $20\,\%$ אפשר לזהות התנהגות המזכירה כיפה של ΔT_c כתלות ברמת האילוח. ההפרש הגדול ביותר בין הטמפרטורות הקריטיות הינו K4.3 והתקבל עבור רמת אילוח של $17\,\%$, קרוב לרמת האילוח האופטימלית של LSCO ($x = 15\,\%$). הכיפה מתחילה לעלות בקרבת נקודה קוונטית קריטית ברמת אילוח של $12.5\,\%$ (אילוח $1/8$) ויורדת בקרבת נקודה קוונטית קריטית אחרת ברמת אילוח של $19\,\%$. התנהגות זו של ΔT_c כתלות באילוח בסביבת הנקודות הקוונטיות הקריטיות יכולה להצביע על קשר בין האנאיזוטרופיות של המערכת לבין תופעות אחרות כמו המעבר בין פאזה של נוזל־פרמי (Fermi liquid) לפאזה של מתכת־מוזרה (strange metal) או לפתיחה של ה"פסודוגאפ" (pseudogap).

על־ידי הגברת הזרם שעובר בסליל העירור ניתן לסחוף את הפוטנציאל הוקטורי המגנטי עד שהקשר הליניארי בין $\boldsymbol{A}$ ו־$\boldsymbol{J}_s$ נשבר. כך ניתן למדוד את צפיפות הזרם הקריטית ללא צורך בהכנת מגעים, ללא תנאים שמחוץ לשיווי משקל טרמי ובהיעדר מערבולות זרם. מדידת צפיפות הזרם הקריטית מיתרגמת גם לחסם עליון על אורך הקוהרנטיות ξ. השתמשנו בסליל עירור על־מוליך עשוי NbTi כדי לבצע מדידות אלו עבור טבעת a ו־c של LSCO עם אילוח־יתר ומצאנו ש־$\xi \leq 4\,\mathrm{nm}$. שיפור נוסף של מערך הניסוי יוכל לספר חסם הדוק יותר על ξ.

תקציר

הקשיחות העל־מוליכה $\hat{\rho}_s$ מביעה את היחס שבין הפוטנציאל הוקטורי המגנטי $\boldsymbol{A}$ וצפיפות הזרם העל־מוליכה $\boldsymbol{J}_s$ בתוך מוליך־על לפי משוואת לונדון $\boldsymbol{J}_s = \hat{\rho}_s \boldsymbol{A}$. אורך הקוהרנטיות הינו מדד לגודל עליו יכולה צפיפות הזרם להתפתח. טכניקה חדשה למדידת הקשיחות העל־מוליכה ואורך הקוהרנטיות הנקראת "קשיחומטר" (Stiffnessometer) פותחה בקבוצת המחקר שלנו. המדידה מתבצעת על־ידי הזרמת זרם חשמלי דרך סליל־עירור דק וארוך העובר דרך דגם על־מוליך בצורת טבעת ומשרה בתוכו פוטנציאל וקטורי מגנטי חסר רוטור $\boldsymbol{A}$. לפי משוואת לונדון מתעוררים בטבעת זרמים על־מוליכים היוצרים מומנט מגנטי אותו ניתן למדוד באמצעות מגנטומטר סקוויד (מכשיר התאבכות קוונטית מוליך־על, SQUID). השיטה החדשה אינה סובלת מסיבוכים של גורם דימגנטיזציה או מקיומם של מערבולות זרם (Vortices).

באמצעות שיטה זו נמדדו דגמים של LSCO ($La_{2-x}Sr_xCuO_4$) ממשפחת הקופרטים. הצורה הגבישית של LSCO הינה תיבתית ובעלת שני צירים סימטריים (ציר־a וציר־b), המקבילים למישורים של נחושת וחמצן CuO_2 וציר נוסף (ציר־c) הניצב למישורים אלו. כתוצאה ממבנה זה, הקשיחות העל־מוליכה הינה אנאיזוטרופית וניתן לצפות לתגובה שונה של הדגם לפוטנציאל וקטורי מגנטי מקביל למישורים לעומת פוטנציאל וקטורי מגנטי הניצב למישורים. כאשר מחממים את הדגם, הקריאה המגנטית נחלשת ולבסוף נעלמת לגמרי כאשר מגיעים לטמפרטורה הקריטית T_c. מדידות קשיחות נעשו על שתי טבעות LSCO עם אילוח של $12.5\,\%$, כאשר באחת הטבעות משורי ה־CuO_2 ניצבים לציר הסימטריה של הטבעת (טבעת־c) ובשנייה המישורים מקבילים לציר הסימטריה של הטבעת (טבעת־a). מתוך מדידות אילו נראה, כי מעבר הפאזה של טבעת־c מתרחש בטמפרטורה הגבוהה ב־$0.7\,\mathrm{K}$ לעומת המעבר של טבעת־a. בעבודה זו יוצגו מדידות קשיחות של טבעות a ו־c עשויות LSCO עבור אחוזי אילוח שונים על־מנת להבין איך האניזוטרופיה של T_c תלויה באילוח.

המחקר נעשה בהנחיית פרופסור עמית קרן בפקולטה לפיזיקה

אני מודה לטכניון על התמיכה הכספית הנדיבה בהשתלמותי

מדידות של תלות

האניזוטרופיה בטמפרטורת

המעבר בסימום, ואורך

הקוהרנטיות ב LSCO

חיבור על מחקר

לשם מילוי חלקי של הדרישות לקבלת התואר מגיסטר

למדעים בפיסיקה

איתי מנגל

הוגש לסנט הטכניון - מכון טכנולוגי לישראל

אלול, התשע"ט, חיפה, ספטמבר, 2019

מדידות של תלות

האניזוטרופיה בטמפרטורת

המעבר בסימום, ואורך

הקוהרנטיות ב LSCO

איתי מנגל